

# Unveiling the flux tube structure in full QCD

M. Baker<sup>a,1</sup>, P. Cea<sup>b,2</sup>, V. Chelnokov<sup>c,3</sup>, L. Cosmai<sup>d,2</sup>, A. Papa<sup>e,4,5</sup>

<sup>1</sup>Department of Physics, University of Washington, WA 98105 Seattle, USA

<sup>2</sup>INFN - Sezione di Bari, I-70126 Bari, Italy

<sup>3</sup>Institut für Theoretische Physik, Goethe Universität, 60438 Frankfurt am Main, Germany

<sup>4</sup>Dipartimento di Fisica dell'Università della Calabria, I-87036 Arcavacata di Rende, Cosenza, Italy

<sup>5</sup>INFN - Gruppo collegato di Cosenza, I-87036 Arcavacata di Rende, Cosenza, Italy

Received: date / Accepted: date

**Abstract** We present lattice Monte Carlo results on the chromoelectric field created by a static quark-antiquark pair in the vacuum of QCD with 2+1 dynamical staggered fermions at physical masses. After isolating the nonperturbative, confining part of the field, we characterize its spatial profile for several values of the physical distances between the sources, ranging from about 0.5 fm up to the onset of string breaking. Moreover, we compare our results with a model of QCD vacuum as disordered chromomagnetic condensate.

## 1 Introduction

Aiming at a deeper understanding of the microscopic mechanisms of confinement, in the recent years we have investigated, by numerical Monte Carlo simulations of the SU(3) pure gauge theory on a space-time lattice, the detailed structure of the color fields in the region around two static sources, a quark and an antiquark, both at zero [1–3] and nonzero temperature [4]. Some of our numerical results have been considered within phenomenological models for hadronization (see, *e.g.*, Refs. [5, 6]).

The following key facts have emerged:

- The (chromo-)magnetic field  $\vec{B}$  around the sources is compatible with zero within uncertainties. The components of the (chromo-)electric field  $\vec{E}$  transverse to the line connecting the sources consist solely of a perturbative, irrotational, short-distance contribution<sup>1</sup>. The longitudinal component of  $\vec{E}$  can be separated into the perturbative,

short-distance part and a nonperturbative term  $\vec{E}^{NP}$ , encoding the confining information, which is shaped as a smooth *flux tube*.

- The curl of the electric field determines a magnetic current  $\vec{J}_{\text{mag}}$  which circulates about the axis of the flux tube and exhibits continuum scaling. The force on the magnetic currents in flux tubes has the form  $\vec{f} = \vec{J}_{\text{mag}} \times \vec{E}^{NP}$ , where  $\vec{J}_{\text{mag}}$  and  $\vec{E}^{NP}$  are measured by lattice simulations, thus supporting the Maxwell picture of confinement [2]. (See also the theoretical analysis of Ref. [7] which states that the longitudinal electric field is dominated by its Abelian components.)

The purpose of the present work is to probe the Maxwell scenario in the case of full QCD with dynamical quarks. Here we expect it to be valid in a manner somewhat similar to the SU(3) pure gauge, as long as the distance between the static sources does not reach the value at which *string breaking* [8–11] occurs and the flux-tube structure disappears. At the onset of the string breaking phenomenon, however, some new features in the behavior of color fields and currents must appear, which can be detected in our numerical simulations.

The paper is organized as follows: in Section 2, we recall the theoretical background of our approach and the Maxwell picture of confinement; in Section 3, we present the setup of our numerical simulations (lattice action, scale setting, smearing procedure); in Section 4, we show our results; in Section 5, we present the basic formulas derived from the model of Ref. [7] to be fitted to numerical data; in Section 6, we discuss possible evidence for string breaking in our numerical data; finally, in Section 7, we draw our conclusions.

<sup>a</sup>e-mail: mbaker4@uw.edu

<sup>b</sup>e-mail: paolo.cea@ba.infn.it

<sup>c</sup>e-mail: chelnokov@itp.uni-frankfurt.de

<sup>d</sup>e-mail: leonardo.cosmai@ba.infn.it

<sup>e</sup>e-mail: alessandro.papa@fis.unical.it

<sup>1</sup>From now on, we omit the prefix "chromo-" for fields.

## 2 Connected correlator, field strength tensor, Maxwell picture of the flux tube

Similarly to our previous studies in SU(3) pure gauge theory [1–3], we determine the spatial distributions of the color fields induced by a static quark-antiquark pair from lattice measurements of the connected correlation function  $\rho_{W,\mu\nu}^{\text{conn}}$  [12] of a plaquette  $U_P = U_{\mu\nu}(x)$  in the  $\mu\nu$  plane, and a square Wilson loop  $W$  (see Fig. 1),

$$\rho_{W,\mu\nu}^{\text{conn}} = \frac{\langle \text{tr}(WLU_P L^\dagger) \rangle}{\langle \text{tr}(W) \rangle} - \frac{1}{N} \frac{\langle \text{tr}(U_P) \text{tr}(W) \rangle}{\langle \text{tr}(W) \rangle}, \quad (1)$$

$N = 3$  being the number of QCD colors. The correlator  $\rho_{W,\mu\nu}^{\text{conn}}$  provides a lattice definition of a gauge-invariant field strength tensor  $\langle F_{\mu\nu} \rangle_{q\bar{q}} \equiv F_{\mu\nu}$  carrying a unit of octet charge, while possessing the space-time symmetry properties of the Maxwell field tensor of electrodynamics,

$$\rho_{W,\mu\nu}^{\text{conn}} \equiv a^2 g \langle F_{\mu\nu} \rangle_{q\bar{q}} \equiv a^2 g F_{\mu\nu}. \quad (2)$$

When the plaquette  $U_P$  lies in the  $\hat{4}\hat{1}$  plane, the measured  $\hat{4}\hat{1}$  component of the field tensor determines  $E_x$ , the component of the electric field along the  $q\bar{q}$  axis  $E_x = F_{41}$ ; *i.e.*, the longitudinal component of the electric field at the position corresponding to the center of the plaquette.

When  $U_P$  is in the  $\hat{4}\hat{2}$  plane,  $F_{42} = E_y$ , a component of the electric field transverse to the  $q\bar{q}$  axis, when  $U_P$  is in the  $\hat{2}\hat{3}$  plane,  $F_{23} = B_x$ , the longitudinal component of the magnetic field, *etc.*

The Maxwell-like field  $F_{\mu\nu}$ , see Eq. (2), generates a magnetic current density  $J_\alpha^{\text{mag}}$  that circulates about the axis of the flux tube:

$$J_\alpha^{\text{mag}} \equiv \frac{1}{2} \varepsilon_{\alpha\beta\mu\lambda} \frac{\partial F_{\mu\lambda}}{\partial x^\beta}, \quad (\varepsilon_{4123} = 1). \quad (3)$$

(The presence of magnetic currents in SU(3) lattice gauge theory was already suggested in Ref. [13].)

The Maxwell stress tensor  $T_{\alpha\beta}$  determines the force density  $f_\beta$  acting on these currents:

$$T_{\alpha\beta} = F_{\alpha\lambda} F_{\beta\lambda} - \frac{1}{4} \delta_{\alpha\beta} F_{\mu\lambda} F_{\mu\lambda}, \quad (4)$$

$$f_\beta = \frac{\partial}{\partial x^\alpha} T_{\alpha\beta} = -F_{\mu\lambda} \frac{1}{2} \varepsilon_{\alpha\beta\mu\lambda} J_\alpha^{\text{mag}}. \quad (5)$$

Under the assumption that the magnetic components of the field tensor,  $\frac{1}{2} \varepsilon_{ijk} F_{jk}$ , vanish, the spatial part of Eq. (3) becomes

$$\vec{J}_{\text{mag}} = \vec{\nabla} \times \vec{E}, \quad (6)$$

while the spatial part of Eq. (5) becomes  $\vec{f} = \vec{J}_{\text{mag}} \times \vec{E}$ .

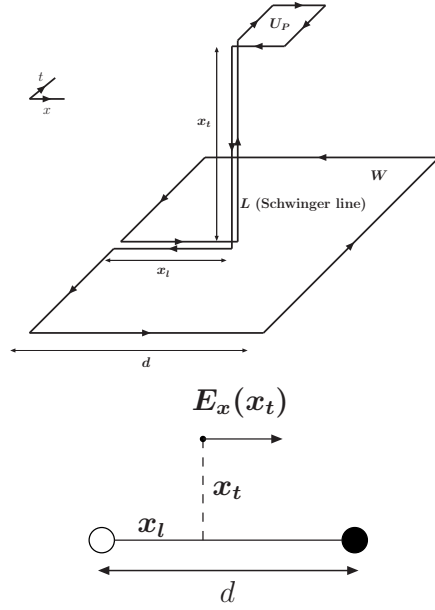


**Figure 1** The connected correlator between the plaquette  $U_P$  and the Wilson loop (subtraction in  $\rho_{W,\mu\nu}^{\text{conn}}$  not explicitly drawn). The longitudinal electric field  $E_x(x_t)$  at some fixed displacement  $x_t$  along the axis connecting the static sources (represented by the white and black circles), for a given value of the transverse distance  $x_t$ .

Replacing the color electric field  $\vec{E}$  by its nonperturbative longitudinal component  $\vec{E}^{\text{NP}}$ , determined from our lattice simulations of the connected correlator, we obtain

$$\vec{f} = \vec{J}_{\text{mag}} \times \vec{E}^{\text{NP}}, \quad (7)$$

the confining force density directed toward the flux-tube axis.

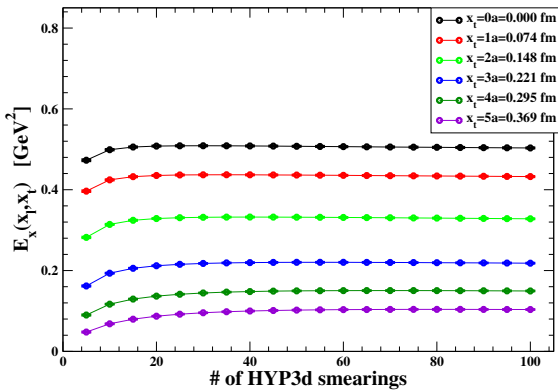
The 'Maxwell' picture of confinement is supported by a recent analysis of the confinement in SU(3) theories [7], showing that the electric field  $gE^a$  in the flux tube is mainly composed of the Abelian components  $gE^3$  and  $gE^8$ .

## 3 Lattice setup and smearing procedure

We perform simulations of lattice QCD with 2+1 flavors of HISQ (Highly Improved Staggered Quarks) quarks. We have made use of the HISQ/tree action [14–16]. Couplings are adjusted so as to move on a line of constant physics (LCP), as determined in Ref. [17], with the strange quark mass  $m_s$  fixed at its physical value and a light-to-strange mass ratio  $m_l/m_s = 1/20$ , corresponding to a pion mass of 160 MeV in the continuum limit. We have simulated the theory for several values of the gauge coupling, adopting lattices of size  $24^4$ ,  $32^4$  and  $48^4$ . The thermalized lattice configurations, stored for further measurements, are each separated by 25 trajectories of rational hybrid Monte Carlo (RHMC) with length one. The electromagnetic field tensor has been measured for a static quark and antiquark placed at a

**Table 1** Summary of the numerical simulations.

lattice	$\beta = 10/g^2$	$a(\beta)$ [fm]	$d$ [lattice units]	$d$ [fm]	statistics
48 <sup>4</sup>	6.885	0.0949777	6	0.569866	500
32 <sup>4</sup>	7.158	0.0738309	8	0.590647	10064
24 <sup>4</sup>	6.445	0.144692	5	0.723462	3330
32 <sup>4</sup>	7.158	0.0738309	10	0.738309	10181
48 <sup>4</sup>	6.885	0.0949777	8	0.75982	779
32 <sup>4</sup>	6.885	0.0949777	8	0.759821	4409
32 <sup>4</sup>	6.5824	0.126658	6	0.759947	2667
32 <sup>4</sup>	6.3942	0.15203	5	0.760151	3000
32 <sup>4</sup>	6.885	0.0949777	9	0.854799	4347
32 <sup>4</sup>	6.25765	0.173715	5	0.868573	3545
32 <sup>4</sup>	6.5824	0.126658	7	0.886605	2667
32 <sup>4</sup>	6.3942	0.15203	6	0.912182	3000
48 <sup>4</sup>	6.885	0.0949777	10	0.949777	779
32 <sup>4</sup>	7.158	0.0738309	13	0.959801	10183
24 <sup>4</sup>	6.445	0.144692	7	1.01285	3330
32 <sup>4</sup>	6.5824	0.126658	8	1.01326	2666
32 <sup>4</sup>	7.158	0.0738309	14	1.03363	2107
32 <sup>4</sup>	6.25765	0.173715	6	1.04229	3549
32 <sup>4</sup>	6.885	0.0949777	11	1.04475	4408
32 <sup>4</sup>	6.3942	0.15203	7	1.06421	3000
32 <sup>4</sup>	6.33727	0.160714	7	1.125	3133
32 <sup>4</sup>	6.885	0.0949777	12	1.13973	4409
48 <sup>4</sup>	6.885	0.0949777	12	1.13973	769
32 <sup>4</sup>	6.5824	0.126658	9	1.13992	2667
32 <sup>4</sup>	6.314762	0.164286	7	1.15	3651
24 <sup>4</sup>	6.445	0.144692	8	1.157536	3330
32 <sup>4</sup>	6.28581	0.168999	7	1.18299	3148
32 <sup>4</sup>	6.25765	0.173715	7	1.216	3546
32 <sup>4</sup>	6.3942	0.15203	8	1.21624	3000
32 <sup>4</sup>	6.885	0.0949777	13	1.23471	4409
32 <sup>4</sup>	6.5824	0.126658	10	1.26658	2667
32 <sup>4</sup>	6.3942	0.15203	9	1.36827	3000

**Figure 2** Behavior under smearing of the "full" longitudinal electric field,  $E_x$ , for different values of the transverse distance  $x_t$ , at  $\beta = 7.158$  and  $d = 10a = 0.74$  fm on a lattice  $32^4$ .

given distance  $d$  in lattice spacing. We fix the lattice spacing

through the observable  $r_1$  as defined in the Appendix B of Ref. [17].

For the  $r_1$  scale the lattice spacing is given in terms of the  $r_1$  parameter as:

$$\frac{a}{r_1}(\beta)_{m_l=0.05m_s} = \frac{c_0 f(\beta) + c_2 (10/\beta) f^3(\beta)}{1 + d_2 (10/\beta) f^2(\beta)}, \quad (8)$$

with  $c_0 = 44.06$ ,  $c_2 = 272102$ ,  $d_2 = 4281$ ,  $r_1 = 0.3106(20)$  fm.

The connected correlator defined in Eq. (1) exhibits large fluctuations at the scale of the lattice spacing, which are responsible for a small signal-to-noise ratio. To extract the physical information carried by fluctuations at the physical scale (and, therefore, at large distances in lattice units), we smoothed out configurations by a *smearing* procedure.

Our setup consisted of one step of 4-dimensional hypercubic smearing [18] on the temporal links (HYPt), with smearing parameters  $(\alpha_1, \alpha_2, \alpha_3) = (1.0, 1.0, 0.5)$ , and  $N_{\text{HYP3d}}$  steps of hypercubic smearing restricted to the three spatial directions (HYP3d) with  $(\alpha_1^{\text{HYP3d}}, \alpha_3^{\text{HYP3d}}) = (0.75, 0.3)$ .

The operator in Eq. (1), which defines the color field strength tensor, undergoes a nontrivial renormalization [19],

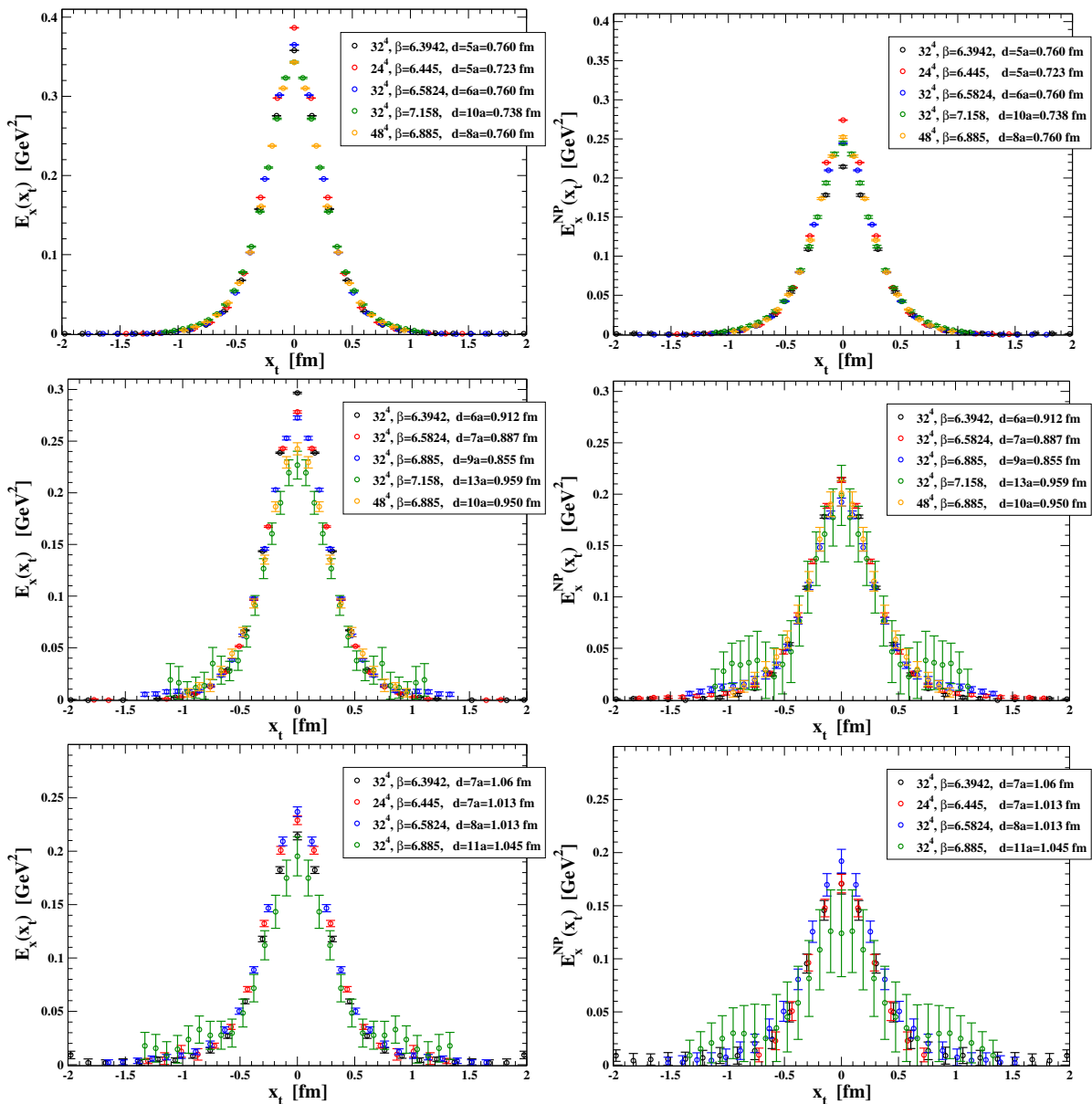


**Figure 3** Scaling test for the full electric field (left panels) and for its nonperturbative part (right panels) on the midplane for distances in the range  $d = 0.723 - 0.760$  fm (upper panels),  $d = 0.855 - 0.959$  fm (middle panels) and  $d = 1.013 - 1.060$  fm (lower panels).

which depends on  $x_t$ . As discussed in Refs. [1, 2], comparing our results with those in Ref. [19], we argued that smearing behaves as an effective renormalization. In Fig. 2 we show an example of the behavior under smearing of the longitudinal component of the electric field at the midplane between the sources and for different values of the transverse position  $x_t$ : initially, smearing erases fluctuations at the level of the lattice spacing and leads to a rapid growth of the signal up to a maximum; thereafter, further smearing results in extended plateaus followed by a slow decrease, due to the fact that finally also the long-distance structure of the signal gets affected and degrades. We choose therefore the *optimal* number of smearing steps as the one for which the field takes

its maximum value. It typically corresponds to a few units at small values of  $x_t$  and to a few tens at larger values of  $x_t$ .

The smearing procedure can also be validated *a posteriori* by the observation of *continuum scaling*, *i.e.*, by checking that fields obtained in the same *physical* setup, but at different values of the coupling and of the optimal number of smearing steps, are in good agreement in the range of gauge couplings used (see subsection 4.1).

In Table 1 we display the list of measurements we have done. We considered distances between the sources in a wide interval, ranging from about 0.57 fm to about 1.37 fm, corresponding to  $\beta$ -values in the range 6.25765 to 7.158.

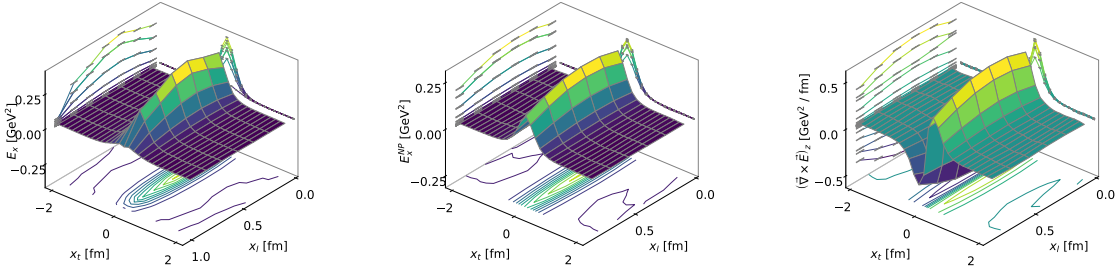


**Figure 4** Space distribution of the full electric field  $E_x$  (left panel) and of its nonperturbative part  $E_x^{NP}$  (middle panel) for  $\beta = 6.3942$  and  $d = 6a = 0.91$  fm. The right panel displays the magnetic current at  $\beta = 6.3942$  and  $d = 0.91$  fm.

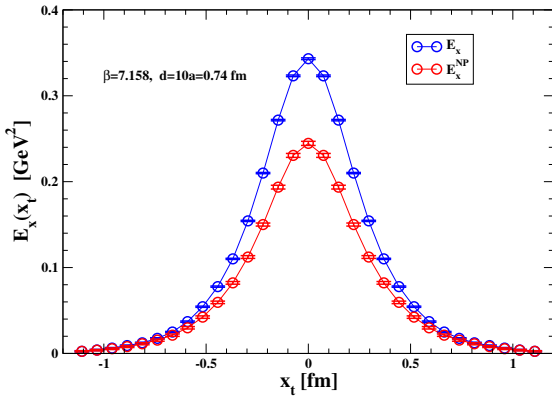


**Figure 5** Space distribution of the full electric field  $E_x$  (left) and of its nonperturbative part  $E_x^{NP}$  (right) for  $\beta = 7.158$  and  $d = 10a = 0.74$  fm in correspondence of the midplane.

## 4 Numerical results

### 4.1 Scaling check

We verified that our lattice setup is close enough to the continuum limit by checking that different choices of the lattice parameters, corresponding to the same physical distance  $d$  between the sources, lead to the same values of the relevant observables when measured in physical units. To this purpose, we considered the full electric field and its nonperturbative part at the midplane between the sources when the distance between the sources is in the range  $d = 0.723 - 0.760$  fm for six different lattice setups, in the range  $d = 0.855 - 0.959$  fm for six different lattice setups and in the range  $d = 1.013 - 1.060$  fm for four different lattice setups, see Fig. 3. In all cases data points obtained on different lattices nicely overlap, taking into account the uncertainties and the spread of the  $d$  values inside each of the three considered ranges. We notice from Fig. 3, middle and lower panels, that the uncertainties become quite sizeable for the largest value of  $d$ , especially in the nonperturbative part. This is a consequence of the degradation of the signal-to-noise ratio

at larger distances, which, in the case of the nonperturbative field, is amplified by the curl subtraction.

### 4.2 3d plots and asymmetry

We extract the nonperturbative part of the longitudinal electric field,  $E_x^{NP}$ , by systematic application of the *curl method*, first introduced in Ref. [2], to which refer for the details of the procedure. In Fig. 4 we present two 3D plots giving the space distribution of the full longitudinal electric field  $E_x$  (left panel) and of its nonperturbative part (middle panel): in the latter, a tube-like shape clearly emerges, fairly uniform in the longitudinal direction, up to a small asymmetry (the field at  $x_l = 0$  is a bit higher than the field at  $x_l = d$ ) probably due to the asymmetric structure of the adopted lattice operator (see Fig. 1), which the smearing procedure is unable to balance. From data for the electric field, the magnetic current, given by the curl of the electric field, can also be extracted. For distances  $d \lesssim 1$  it is a smooth function, see Fig. 4, right panel, for an example.

In Fig. 5 we show a transverse section of the electric field profile, comparing its full value and the nonperturbative part at the midplane between the sources: the latter is sensibly smaller at  $x_l = 0$ , *i.e.*, on the longitudinal axis, but is roughly as wide as the full one.

### 4.3 Field integrals: string tension and width of the flux tube

To characterize quantitatively the shape and some properties of the flux tube formed by the longitudinal electric field, we calculated numerically the following two expressions, involving three different integrals,

$$\sigma_{\text{eff}} = \int d^2x_t \frac{(E_x^{\text{NP}}(x_t))^2}{2}, \quad (9)$$

$$w = \sqrt{\frac{\int d^2x_t x_t^2 E_x^{\text{NP}}(x_t)}{\int d^2x_t E_x^{\text{NP}}(x_t)}}, \quad (10)$$

**Table 2** Numerical results for  $\sqrt{\sigma_{\text{eff}}}$  and  $w$ , as defined in Eqs. (9) and (10).

lattice	$\beta = 10/g^2$	$a(\beta)$ [fm]	$d$ [lattice units]	$d$ [fm]	$\sqrt{\sigma_{\text{eff}}}$	$w$
48 <sup>4</sup>	6.885	0.0949777	6	0.569866	0.33245(21)	0.65(8)
32 <sup>4</sup>	7.158	0.0738309	8	0.590647	0.40933(6)	0.474(26)
24 <sup>4</sup>	6.445	0.144692	5	0.723462	0.39977(8)	0.46(5)
32 <sup>4</sup>	7.158	0.0738309	10	0.738309	0.38097(26)	0.50(6)
48 <sup>4</sup>	6.885	0.0949777	8	0.75982	0.38470(19)	0.46(7)
32 <sup>4</sup>	6.885	0.0949777	8	0.759821	0.38018(21)	0.46(6)
32 <sup>4</sup>	6.5824	0.126658	6	0.759947	0.38227(12)	0.30(12)
32 <sup>4</sup>	6.3942	0.15203	5	0.760151	0.37420(7)	0.51(5)
32 <sup>4</sup>	6.885	0.0949777	9	0.854799	0.3526(6)	0.71(19)
32 <sup>4</sup>	6.25765	0.173715	5	0.868575	0.35853(12)	0.37(7)
32 <sup>4</sup>	6.5824	0.126658	7	0.886605	0.3715(4)	0.74(31)
32 <sup>4</sup>	6.3942	0.15203	6	0.912182	0.35455(32)	0.56(14)
48 <sup>4</sup>	6.885	0.0949777	10	0.949777	0.3707(18)	0.53(24)
32 <sup>4</sup>	7.158	0.0738309	13	0.959801	0.368(5)	0.61(27)
32 <sup>4</sup>	6.25765	0.173715	6	1.04229	0.3369(8)	0.44(10)
32 <sup>4</sup>	6.885	0.0949777	11	1.04475	0.293(6)	0.62(34)
32 <sup>4</sup>	6.3942	0.15203	7	1.06421	0.3071(18)	0.50(18)

**Table 3** Numerical results for  $\sqrt{\sigma_{\text{eff}}}$  and  $w$ , as defined in Eqs. (9) and (10) with the replacement of the nonperturbative field with the full one.

lattice	$\beta = 10/g^2$	$a(\beta)$ [fm]	$d$ [lattice units]	$d$ [fm]	$\sqrt{\sigma_{\text{eff}}}$	$w$
48 <sup>4</sup>	6.885	0.0949777	6	0.569866	0.48918(18)	0.62(7)
32 <sup>4</sup>	7.158	0.0738309	8	0.590647	0.605219(33)	0.447(18)
24 <sup>4</sup>	6.445	0.144692	5	0.723462	0.53767(5)	0.436(35)
32 <sup>4</sup>	7.158	0.0738309	10	0.738309	0.52234(13)	0.47(4)
48 <sup>4</sup>	6.885	0.0949777	8	0.75982	0.51466(11)	0.45(5)
32 <sup>4</sup>	6.885	0.0949777	8	0.759821	0.51557(10)	0.44(4)
32 <sup>4</sup>	6.5824	0.126658	6	0.759947	0.52667(5)	0.36(8)
32 <sup>4</sup>	6.3942	0.15203	5	0.760151	0.516572(32)	0.459(26)
32 <sup>4</sup>	6.885	0.0949777	9	0.854799	0.45568(28)	0.55(11)
32 <sup>4</sup>	6.25765	0.173715	5	0.868575	0.47216(5)	0.34(4)
32 <sup>4</sup>	6.5824	0.126658	7	0.886605	0.45257(17)	0.32(30)
32 <sup>4</sup>	6.3942	0.15203	6	0.912182	0.46500(12)	0.16(5)
48 <sup>4</sup>	6.885	0.0949777	10	0.949777	0.4273(10)	0.49(20)
32 <sup>4</sup>	7.158	0.0738309	13	0.959801	0.4008(18)	0.50(15)
32 <sup>4</sup>	6.25765	0.173715	6	1.04229	0.37883(27)	0.42(5)
32 <sup>4</sup>	6.885	0.0949777	11	1.04475	0.3550(26)	0.58(20)
32 <sup>4</sup>	6.3942	0.15203	7	1.06421	0.3759(6)	0.47(8)
32 <sup>4</sup>	6.33727	0.160714	7	1.125	0.3151(27)	0.57(33)
32 <sup>4</sup>	6.314762	0.164286	7	1.15	0.4258(35)	0.44(17)
24 <sup>4</sup>	6.445	0.144692	8	1.157536	0.426(5)	0.60(27)

with the longitudinal electric field taken at the midplane between the sources. The first of them represents a quantity which has the dimension of an energy per unit length, similarly to the string tension. However, this quantity, denoted by  $\sigma_{\text{eff}}$ , does not coincide with the true string tension, for which the integrand would contain  $\sum_{a=1}^8 (E_x^a)^2$ . In (9) we have instead the squared Maxwell-like field, which is arguably a linear combination of the Abelian color components 3 and 8 of the electric field (see next Section). The expression in Eq. (10) gives an estimate of the width of the flux tube.

The integrals in Eqs. (9), (10) are computed numerically by means of the trapezoidal rule. They were considered both

for the nonperturbative part of the longitudinal electric field and for the full field. The numerical results are displayed, respectively, in Tables 2 and 3.

In Fig. 6, left panel, we compare the behavior of  $\sigma_{\text{eff}}$  with the distance  $d$  between the sources for the full longitudinal electric field and its nonperturbative part: while for the full field  $\sigma_{\text{eff}}$  tends to decrease, for the nonperturbative part it is fairly stable. This different behavior is not surprising: the full field on the midplane contains also the perturbative contribution, which becomes less and less relevant when the distance between the sources increases. While not visible on the figure, the uncertainties in the estimation of the string ten-

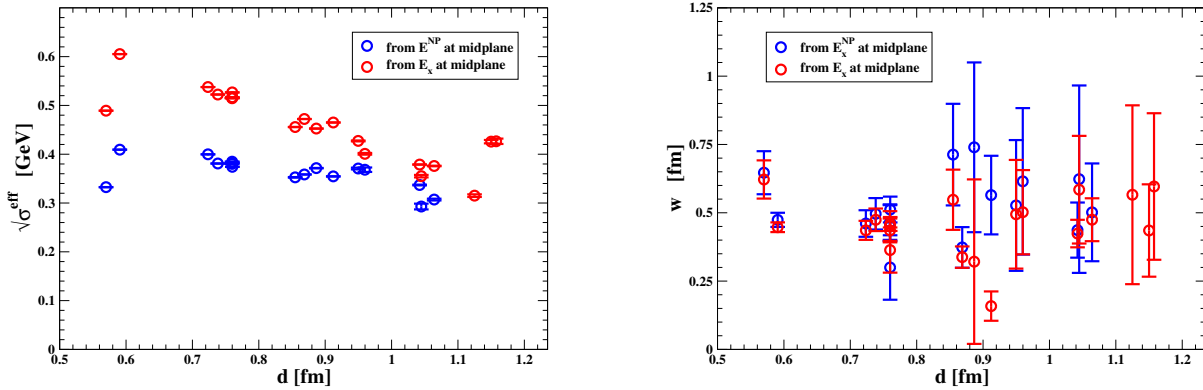


**Figure 6** Behaviour of  $\sigma_{\text{eff}}$  (left panel) and  $w$  (right panel) with the distance  $d$  between the sources, for the full longitudinal electric field (red circles) and its nonperturbative part (blue circles).

sion increase up to two orders, when the distance  $d$  between sources increases, as can be seen in Tables 2 and 3.

In Fig. 6, right panel, we show a similar comparison for the width. Differently from the case of  $\sigma_{\text{eff}}$ , within uncertainties which increase with  $d$ , the width of the flux tube remains stable on a wide range of distances and is generally compatible for the full and the nonperturbative field. The uncertainties in the estimation of the width are much larger than the ones for the estimation of the string tension, due to the fact that the width is defined as a ratio of two numerical integrals.

From the constant fit of the data for string tension and string width we get  $\sqrt{\sigma_{\text{eff}}} \approx 0.4$  GeV, and  $w \approx 0.5$  fm.

## 5 Magnetic currents and electric fields

We have seen how the Maxwell picture of the flux tube leads to a well-defined mechanism for the squeezing of the electric fields into a narrow flux tube. More precisely, the presence of a magnetic current density that circulates around the axis of the flux tube ensures the squeezing of the electric flux tube in the transverse direction according to the Maxwell equation, Eq. (6), that for later convenience we rewrite here as:

$$\vec{\nabla} \times \vec{E}(\vec{x}) = \vec{J}_{\text{mag}}(\vec{x}) . \quad (11)$$

Indeed, if in cylindrical coordinates:

$$\vec{J}_{\text{mag}}(\vec{x}) \simeq J_{\text{mag}}(x_t) \hat{\phi} \quad (12)$$

and the function  $J_{\text{mag}}(x_t)$  decreases sufficiently fast toward zero when  $x_t \rightarrow \infty$ , then Eq. (11) assures the presence of an almost uniform and narrow longitudinal electric field along the flux tube. Actually, the general solution of Eq. (11) is given by:

$$\vec{E}(\vec{x}) = \vec{E}^{\text{NP}}(\vec{x}) + \vec{E}_C(\vec{x}) , \quad (13)$$

where  $\vec{E}_C(\vec{x})$  is the solution of the homogeneous equation  $\vec{\nabla} \times \vec{E}_C(\vec{x}) = 0$  and  $\vec{E}^{\text{NP}}(\vec{x})$  satisfies the nonhomogeneous equation:

$$\vec{\nabla} \times \vec{E}^{\text{NP}}(\vec{x}) = \vec{J}_{\text{mag}}(\vec{x}) . \quad (14)$$

This last equation shows that the nonperturbative electric fields  $\vec{E}^{\text{NP}}(\vec{x})$  turn out to be squeezed into a narrow flux tube leading to a nonzero string tension. Our previous nonperturbative and model-independent analysis allowed to evaluate the Coulomb field  $\vec{E}_C(\vec{x})$  by solving numerically  $\vec{\nabla} \times \vec{E}(\vec{x}) = 0$  and, after that, to determine the nonperturbative electric field by means of Eq. (13). Moreover, by evaluating numerically the curl of the full electric field, we were able to check the validity of Eq. (12) and to track the transverse distribution of the magnetic current. To make further progress, we need some theoretical input on the structure of the magnetic currents. Recently, a first principle attempt to characterize the structure of the QCD vacuum at large distances has been advanced in Ref. [7]. According to Ref. [7], the QCD vacuum resembles a disordered magnetic condensate with average strength  $\sqrt{gH_0} \sim 1.0$  GeV such that color confinement is assured by the presence of a mass gap together with the lack of color long-range order. Interestingly enough, in Ref. [7] there is a physical picture for the formation of the flux tube between static color sources. As a matter of fact, the presence of a static quark-antiquark pair leads to the polarization of the magnetic domains characterizing the QCD vacuum, such that there are magnetic currents circulating around the line joining the static color charges that, in turn, give rise to a Lorentz force that is able to squeeze the electric fields generated by the quark-antiquark pair. More importantly, it turned out that, within the approximations adopted in Ref. [7] and sufficiently far from the color sources, the induced magnetic currents belong to the maximal Abelian subgroup of the

$x_t$ [fm]	$v_\phi$	$\sqrt{gH_0}$ [GeV]	$\alpha$	$\chi_r^2$
0.076	0.079(24)	1.04(13)	0.82(17)	1.98
0.228	0.120(10)	0.908(28)	1.0	1.53
0.380	0.22(11)	0.73(12)	1.4(6)	1.03
0.532	0.20(6)	0.72(8)	1.4(4)	1.03
0.684	0.13(5)	0.83(10)	1.02(28)	0.19
0.836	0.081(21)	0.97(9)	0.81(15)	1.22
0.988	0.068(9)	0.94(5)	1.0	1.42

**Table 4** Values of the parameters for the fits of the lattice data to Eq. (19) along the flux tube at  $\beta = 6.3942$ ,  $a(\beta) \simeq 0.15203$  fm, corresponding to static color source distance  $d = 7a \simeq 1.064$  fm.

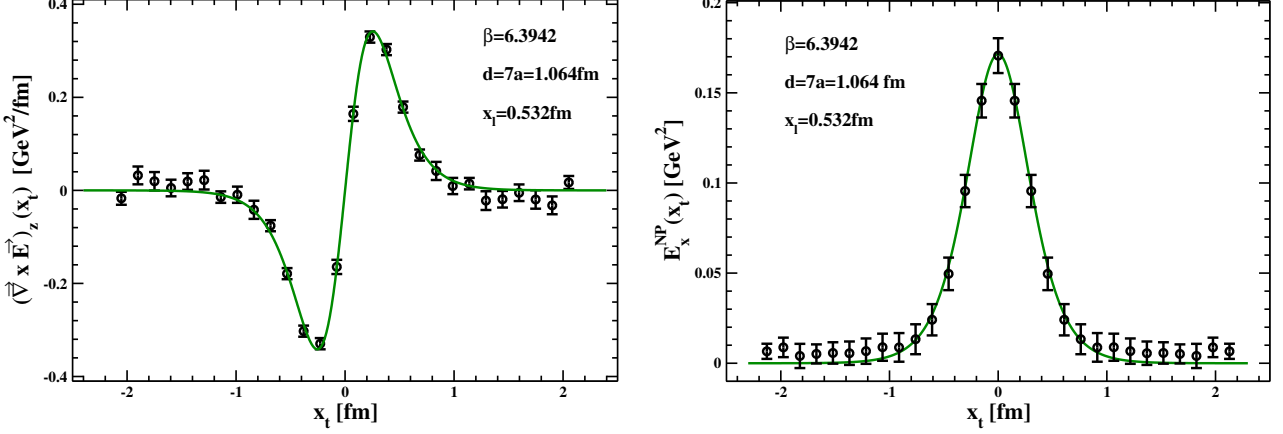


**Figure 7** (Left panel) The lattice data for the curl of the electric field compared to the total magnetic current (full green line). (Right panel) Comparison of the transverse distribution of the nonperturbative flux-tube electric field to  $E_{th}(x_t)$ , Eq. (21) (full green line).

SU(3) gauge group. As a consequence, the equations relating the magnetic currents to the flux-tube electric fields are the familiar Maxwell equations generalised to the case of the presence of magnetic charges [20]:

$$-\vec{\nabla} \times \vec{E}^a(\vec{x}) = \vec{J}_M^a(\vec{x}) . \quad (15)$$

Far from the color sources one has:

$$\vec{J}_M^a(\vec{x}) \simeq \delta^{a3} \vec{J}_M^3(\vec{x}) + \delta^{a8} \vec{J}_M^8(\vec{x}) , \quad (16)$$

where  $\vec{J}_M^{3,8}(\vec{x})$  are azimuthal magnetic currents with strengths [7]:

$$J_M^3(\vec{x}) \simeq -v_\phi \sqrt{2} (gH_0)^{\frac{3}{2}} \frac{\tanh\left(\sqrt{\frac{gH_0}{2}} x_t\right)}{\cosh^2\left(\sqrt{\frac{gH_0}{2}} x_t\right)} , \quad (17)$$

and

$$J_M^8(\vec{x}) \simeq -v_\phi \frac{\sqrt{3}}{2} (gH_0)^{\frac{3}{2}} \frac{\tanh\left(\alpha \sqrt{\frac{gH_0}{4}} x_t\right)}{\cosh^2\left(\alpha \sqrt{\frac{gH_0}{4}} x_t\right)} . \quad (18)$$

In Eq. (17) and Eq. (18)  $v_\phi$  is the azimuthal velocity of the polarised magnetic domains.

Note that the magnetic currents basically depend only on two parameters, *i.e.*,  $v_\phi$  and  $\sqrt{gH_0}$ . However, we have added one

more parameter  $\alpha$  that away from the static color sources should be  $\alpha \simeq 1$  [7]. As we shall see later on, this new parameter will allow us to track the lattice data for the curl of the electric field even near the color sources. According to Ref. [7] the total magnetic current is:

$$J_{\text{mag}}(x_t) \simeq -J_M^3(x_t) - J_M^8(x_t) . \quad (19)$$

Having an explicit expression for the current allows us to find the confining electric field:

$$E^{\text{NP}}(x_t) \simeq E_{\text{th}}(x_t) , \quad (20)$$

with

$$E_{\text{th}}(x_t) \simeq E_{\text{th}}^3(x_t) + E_{\text{th}}^8(x_t) , \quad (21)$$

where

$$E_{\text{th}}^3(x_t) \simeq v_\phi gH_0 \frac{1}{\cosh^2\left(\sqrt{\frac{gH_0}{2}} x_t\right)} \quad (22)$$

and

$$E_{\text{th}}^8(x_t) \simeq \frac{\sqrt{3}}{2\alpha} v_\phi gH_0 \frac{1}{\cosh^2\left(\alpha \sqrt{\frac{gH_0}{4}} x_t\right)} . \quad (23)$$

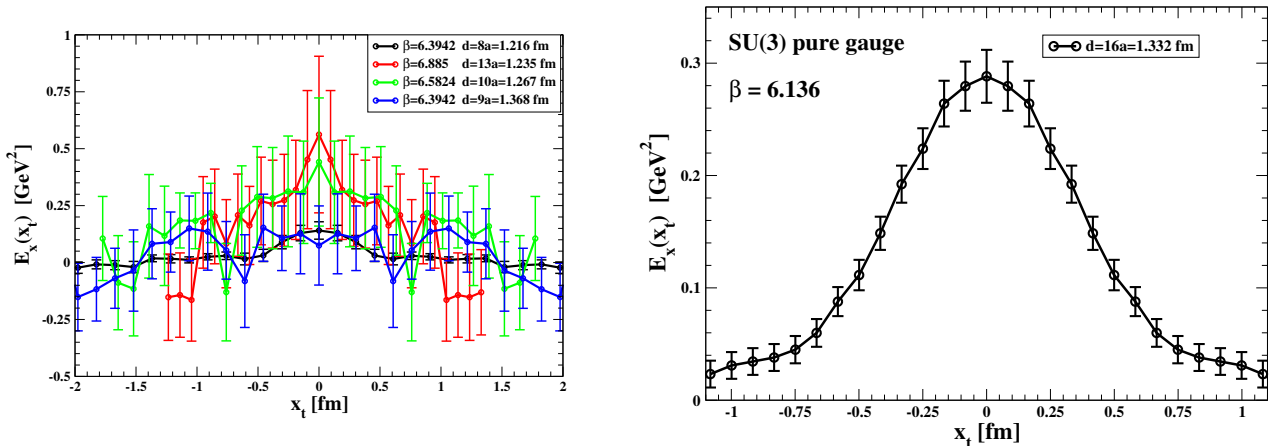


**Figure 8** Transverse profiles of the full longitudinal electric field on the midplane, for various distances between the sources.

A few comments are in order. Firstly, the Abelian nature of the confining electric fields supports our simplified Maxwell approach. The total magnetic current, Eq. (19), depends on three parameters that can be fixed by performing a best fit to the lattice data. After that, one can contrast Eq. (21) to the lattice data. In this way we reach a nontrivial consistency check of our subtraction procedure to extract the nonperturbative electric field and, at the same time, of our Maxwell picture for confinement. Indeed, we have fitted our lattice data for the curl of the electric field to Eq. (19). We found that, indeed, the total magnetic current Eq. (19) tracks quite well the lattice data for values of the distance between the quark-antiquark static pair up to about 1.1 fm (larger distances will be discussed in the following Section). As an explanatory example, in Table 4 we report the best-fit parameters  $v_\phi$ ,  $\sqrt{gH_0}$  and  $\alpha$  along the flux tube corresponding to distance  $d \simeq 1.064$  fm. Also, for illustrative purpose, in Figure 7, left panel, we compare the best-fitted magnetic current to the lattice data.

Once the parameters in the magnetic current have been fixed by the best-fitting procedure, we have a prediction for the non-perturbative confining electric field, Eqs. (21)-(23). In fact, from the right panel in Figure 7 we see that  $E_{\text{th}}(x_t)$  agrees almost perfectly with the data, confirming the consistency of our model-independent numerical procedure to extract the nonperturbative field from the full flux-tube electric field.

## 6 Possible evidence for string breaking

Although our numerical setup is not tailored for a clear-cut detection of the expected *string breaking*, we tried to push our numerical simulations to distances as large as  $\sim 1.37$  fm, searching for hints of this phenomenon. Indeed, in the presence of light quarks it is expected that the string between the static quark-antiquark pair breaks at large distance due

to creation of a pair of light quarks which recombine with the static quarks into two static-light mesons. This expected zero-temperature phenomenon has proven elusive in simulations of lattice QCD and could not be clearly observed in early lattice simulations [21, 22]. Usually, the string breaking distance  $d^*$  is defined as the point where the Wilson loop and the static-light meson operator have equal overlap onto the ground state, *i.e.*, the mixing is most pronounced. Using this method, evidence for string breaking was first found in Ref. [10] for  $N_f = 2$  QCD on the lattice with pion mass about 640 MeV. The authors of Ref. [10] reported a string breaking distance  $d^* \simeq 1.248(13)$  fm. A more recent analysis employed  $N_f = 2+1$  flavors of nonperturbatively improved dynamical Wilson fermions using an ensemble of gauge configurations generated through the Coordinated Lattice Simulations (CLS) effort with pion and kaon mass about 280 MeV and 460 MeV, respectively [23]. By employing the Stochastic Laplacian Heaviside (LapH) method in order to efficiently calculate the correlation functions required for string breaking and performing a variational analysis to extract the ground state as well as the first and second excited state of the system containing two static quarks, the authors of Ref. [23] reported a string breaking distance  $d^* \approx 1.216$  fm. Note that this last estimate is slightly smaller than the one in Ref. [10], as expected since the string breaking distance should decrease with the sea quark mass.

The main advantage of the present paper resides on the fact that we can look directly at the nonperturbative gauge-invariant longitudinal electric field,  $\vec{E}^{\text{NP}}$ , in the region between two static sources that is responsible for the formation of a well-defined flux tube, characterized by nonzero effective string tension  $\sigma_{\text{eff}}$  and width  $w$ . To this end, in Fig. 8, left panel, we show the transverse profile of the full longitudinal electric field on the midplane between two sources located at distances of 1.216 fm, 1.235 fm, 1.267 fm and 1.368 fm: at

the latter distance the signal is almost completely lost. One might object that this is the effect of a degradation of the signal-to-noise ratio, due to the increasing distance *in lattice units*. This is however contradicted by the fact that at much larger values of the distance in lattice units, but a smaller physical distance, the signal is clearly present, see data for  $d = 1.235$  fm, corresponding to 13 lattice spacings, in Fig. 8, left panel.

Even though for  $1.216 \text{ fm} \lesssim d < 1.368 \text{ fm}$  we found evidence for the nonzero full longitudinal electric field on the mid-plane between two sources, we found no signs of a sizeable *nonperturbative* longitudinal electric field. This led us to extend the previous analysis to the smaller distances  $d \simeq 1.140 \text{ fm}$ ,  $1.157 \text{ fm}$ ,  $1.183 \text{ fm}$  (see Table 1). Even in these cases, after subtracting the perturbative field from the full longitudinal electric field we found no clear evidence of a non-zero nonperturbative electric field. In other words, for  $d \gtrsim 1.140 \text{ fm}$  we see no indication of the formation of the flux tube between the two color static sources.

Other facts that we observed are the following:

- when the physical distance between quarks  $d$  exceeds a certain value  $d^*$ , our method for the extraction of the longitudinal nonperturbative electric field  $E_x^{\text{NP}}$  fails, due to the large uncertainties. Taking into account that we have a well-defined nonperturbative flux tube up to  $d \simeq 1.064 \text{ fm}$  (see the last entry in Table 2), and above  $d \simeq 1.140 \text{ fm}$  we cannot estimate the nonperturbative field, we can give a rough estimate of this distance as  $1.064 \text{ fm} \lesssim d^* \lesssim 1.140 \text{ fm}$ . Note that our estimation seems to be somewhat smaller with respect to Ref. [23], due to the fact that we are considering QCD with (2+1) dynamical fermions at physical masses. Actually, our determination of the string breaking distance is still slightly smaller with respect to the recent estimate extrapolated to the physical light-quark masses presented in Ref. [24], but in good agreement with the estimate of the string breaking distance extrapolated to real QCD of Ref. [10];
- above  $d^*$ , no improvement can be observed if the distance in lattice units is reduced, keeping  $d^*$  fixed;
- in SU(3) pure gauge theory by definition the string is unbroken. Here, at the physical distances  $d \sim d^*$  the signal is still there, see Fig. 8, right panel.

In our approach, the string breaking distance  $d^*$  should manifest in the drop of the (nonperturbative) electric field, and thus the decrease of the effective string tension  $\sqrt{\sigma_{\text{eff}}}$ . Although our numerical data does not show a clear drop in  $\sqrt{\sigma_{\text{eff}}}$ , the fact that above  $d^*$  our method fails in the 2+1 flavour QCD, but not in the pure gauge theory, can itself be a sign of the string breaking.

From this analysis, we cannot make any firm claim about the onset of string breaking. We have just provided with some indirect hints of its appearance, which need to be corroborated by further tests.

## 7 Conclusions

We have investigated, by Monte Carlo numerical simulations of QCD with (2+1) dynamical staggered fermions at physical masses, the behavior of the nonperturbative gauge-invariant longitudinal electric field,  $\bar{E}^{\text{NP}}$ , in the region between two static sources, a quark and an antiquark.

We have performed our numerical simulations for a range of values of the coupling where continuum scaling is satisfied and have considered several values of the physical distance between the sources, ranging from about 0.5 fm up to about 1.37 fm. Although our simulations allow us to depict the spatial distribution of all color fields in the region between the sources, for the sake of clarity and simplicity, most of the results presented in this paper refer to the transverse plane midway between the sources.

Our findings can be summarized as follows.

After subtraction of the perturbative component, the longitudinal electric field takes the shape of a flux tube, whenever the distance between the sources does not exceed a value  $d^* \simeq 1.1 \text{ fm}$ . This flux tube can be characterized by two quantities,  $\sigma_{\text{eff}}$ , which is related to the string tension, and the width  $w$ , which we have determined by numerical integration of our lattice data for the electric field at the midplane between the sources.

Above the distance  $d^*$ , the longitudinal nonperturbative field is always compatible with zero, within large numerical uncertainties. Our approach does not permit us to conclude if the disappearance of the nonperturbative signal at large distances is due to a signal-to-noise degradation or if it is instead a manifestation of the expected phenomenon of *string breaking*. We have provided some numerical arguments in favor of the latter hypothesis, but plan to corroborate them with future investigations.

We have compared our findings with a model of the QCD vacuum as disordered magnetic condensate, finding a good compatibility between predictions and numerical results.

We plan to extend this analysis to the case of QCD with (2+1) flavors at nonzero temperature and density.

## Acknowledgements

This investigation was in part based on the MILC collaboration’s public lattice gauge theory code (<https://github.com/milc-qcd/>). Numerical calculations have been made possible through a CINECA-INFN agreement, providing access to HPC resources at CINECA. PC, LC and AP acknowledge support from INFN/NPQCD project. VC acknowledges support by the Deutsche Forschungsgemeinschaft (DFG, German Research Foundation) through the CRC-TR 211 “Strong-interaction matter under extreme conditions” – project number 315477589 – TRR 211. This work is (partially) supported by ICSC – Centro Nazionale di Ricerca in

High Performance Computing, Big Data and Quantum Computing, funded by European Union – NextGenerationEU.

## References

1. M. Baker, P. Cea, V. Chelnokov, L. Cosmai, F. Cuteri, A. Papa, *Eur. Phys. J. C* **79**, 478 (2019), 1810.07133
2. M. Baker, P. Cea, V. Chelnokov, L. Cosmai, F. Cuteri, A. Papa, *Eur. Phys. J. C* **80**, 514 (2020), 1912.04739
3. M. Baker, V. Chelnokov, L. Cosmai, F. Cuteri, A. Papa, *Eur. Phys. J. C* **82**, 937 (2022), 2207.08797
4. M. Baker, V. Chelnokov, L. Cosmai, F. Cuteri, A. Papa, *Eur. Phys. J. C* **84**, 150 (2024), 2310.04298
5. C. Bierlich, S. Chakraborty, G. Gustafson, L. Lönnblad, *SciPost Phys.* **13**, 023 (2022), 2202.12783
6. C. Bierlich, S. Chakraborty, G. Gustafson, L. Lönnblad, *JHEP* **03**, 270 (2021), 2010.07595
7. P. Cea, *Universe* **2024**, 10, 111 (2024), 2311.14791
8. O. Philipsen, H. Wittig, *Phys. Rev. Lett.* **81**, 4056 (1998), [Erratum: *Phys. Rev. Lett.* **83**, 2684 (1999)], hep-lat/9807020
9. S. Kratochvila, P. de Forcrand, *Nucl. Phys. Proc. Suppl.* **119**, 670 (2003), [,670(2002)], hep-lat/0209094
10. G.S. Bali, H. Neff, T. Duessel, T. Lippert, K. Schilling (SESAM), *Phys. Rev.* **D71**, 114513 (2005), hep-lat/0505012
11. V. Koch, J. Bulava, B. Hörz, F. Knechtli, G. Moir, C. Morningstar, M. Peardon, *PoS LATTICE2015*, 100 (2016), 1511.04029
12. A. Di Giacomo, M. Maggiore, S. Olejnik, *Phys. Lett.* **B236**, 199 (1990)
13. P. Skala, M. Faber, M. Zach, *Nucl.Phys.* **B494**, 293 (1997), hep-lat/9603009
14. E. Follana et al. (HPQCD Collaboration, UKQCD Collaboration), *Phys.Rev.* **D75**, 054502 (2007), hep-lat/0610092
15. A. Bazavov et al. (MILC), *Rev. Mod. Phys.* **82**, 1349 (2010), 0903.3598
16. A. Bazavov et al. (MILC), *Phys. Rev.* **D82**, 074501 (2010), 1004.0342
17. A. Bazavov et al., *Phys. Rev.* **D85**, 054503 (2012), 1111.1710
18. A. Hasenfratz, F. Knechtli, *Phys. Rev.* **D64**, 034504 (2001), hep-lat/0103029
19. N. Battelli, C. Bonati, *Phys. Rev.* **D99**, 114501 (2019), 1903.10463
20. J.D. Jackson, *Classical electrodynamics*, 3rd edn. (Wiley, New York, NY, 1999), ISBN 9780471309321, <http://cdsweb.cern.ch/record/490457>
21. E. Laermann, C.E. DeTar, O. Kaczmarek, F. Karsch, *Nucl. Phys. B Proc. Suppl.* **73**, 447 (1999), hep-lat/9809105
22. S. Kratochvila, P. de Forcrand, *Nucl. Phys. B* **671**, 103 (2003), hep-lat/0306011
23. V. Koch, J. Bulava, B. Hörz, F. Knechtli, G. Moir, C. Morningstar, M. Peardon, *PoS LATTICE2018*, 053 (2018), 1811.09289
24. J. Bulava, F. Knechtli, V. Koch, C. Morningstar, M. Peardon, *Phys. Lett. B* **854**, 138754 (2024), 2403.00754